Engineering Structures 318 (2024) 118705

Contents lists available at ScienceDirect

Engineering Structures

journal homepage: www.elsevier.com/locate/engstruct

Novel bamboo-raft-type floating structure (BRT-FS) assembled by FRP reinforced concrete tubes: Conceptual design and analysis

Chongfeng Xie, Peng Feng *

MOE Key Lab of Civil Engineering Safety and Durability, Department of Civil Engineering, Tsinghua University, Beijing, 100084, China

ARTICLE INFO

Keywords:
Bamboo-raft-type
Floating structure
Concrete
Fiber reinforced polymer (FRP)

ABSTRACT

To improve construction efficiency in offshore engineering and extend service life of offshore platforms, a novel bamboo-raft-type floating structure (BRT-FS) assembled by FRP reinforced concrete tubes is proposed. It comprises four fundamental components: concrete tube, carbon fiber-reinforced polymer (CFRP) cable, holding beam, and bellow. This paper presents the structure system and structure design of BRT-FS. Separating load-bearing and buoyant functions ensures structural safety and ease of design. It has broad application perspectives in offshore construction due to its high corrosion resistance, designability, construction efficiency, and low crack control requirement. Furthermore, to obtain the operation conditions of BRT-FS, the mechanical performance is analyzed from two levels, which are hydroelastic analysis and structural analysis. Hydroelastic analysis is conducted under different wave directions, wave periods, water depths, and structural dimensions using a new finite element-boundary element (FE-BE) method. In a specify study case, a sensitive period around 11 s for head sea, around 7 s for oblique wave, around 5 s for beam sea are noted. The hydroelastic response is not significantly affected by water depth or transverse dimension. Structural analysis indicates that the structure can work in clam harbour sea with breakwater protection. Even after concrete tubes crack in higher waves, this new structure can still float with the inside bellows in theory. These preliminary findings confirm the feasibility of this novel structure. Structural details such as tube-tube joints, tube-beam joints, CFRP cable anchorages, and other connections will be further designed and tested in the future.

1. Introduction

Ocean contains a considerable number of resources. The fast-growing marine industries, such as aquaculture, oil, and gas exploitation, reflect enormous economic value[8,16]. Besides, Climate change and urban development have also further fuelled the need to utilize ocean space. Some large floating city concepts, such as Oceanix City, have even been proposed[36]. With the economic development of coastal cities and the progress of ocean engineering technology, floating platforms will enter a boom.

Compared with steel, the construction of floating platforms with concrete is characterized by outstanding durability, high load-bearing capacity, and excellent dynamic performance[27]. Many concrete floating platform concepts have been proposed and even put into application. In 1995, Troll B, the first concrete semi-submersible platform was built in the North Sea, with a displacement of 193,000 tons [10]. Another type of floating concrete structures extensively explored is the EPS-concrete system[18]. Expanded polystyrene (EPS) provides buoyancy, while the concrete frame provides stiffness. Besides these existing structures, several new concepts of modular concrete floating structures have also been proposed. Rectangular or hexagon modules are used to form whole structures through connector systems[12–14,5]. Furthermore, Li et al. introduced fiber-reinforced polymer (FRP) and ultra-high performance concrete (UHPC) into concrete floating structures[22].

In addition to concrete, FRP composite is also an ideal offshore construction material. FRP composite consists of fibers and resin matrix, known for its lightweight, high strength, and corrosion resistance[24]. These properties make it have been applied widely in piles, pipelines, offshore platforms, and other offshore engineering[20,3,38,7].

The disadvantages of steel reinforced concrete structures, such as heavy and easy cracking, limit their wide application in offshore engineering. Replacing steel bars and cables with FRP bars and cables can effectively breakthrough this obstacle. Firstly, glass FRP (GFRP) surpasses steel with a strength-to-density ratio over 5 times higher, while carbon FRP (CFRP) exceeds steel by over 16 times. Employing FRP

* Corresponding author.
E-mail address: fengpeng@tsinghua.edu.cn (P. Feng).

https://doi.org/10.1016/j.engstruct.2024.118705
Received 9 January 2024; Received in revised form 8 June 2024; Accepted 25 July 2024
Available online 1 August 2024
0141-0296/© 2024 Elsevier Ltd. All rights are reserved, including those for text and data mining, AI training, and similar technologies.

composites can effectively decrease the deadweight of platform. Secondly, steel reinforced concrete needs to be provided with a certain thickness of protective layer due to the effects of chloride ion erosion and carbonation. For tidal and splash zones, both Chinese and Norwegian standards specify a concrete protective layer thickness of 50 mm. In practice, this protective layer thickness even extends up to 75 mm[11]. FRP reinforcement can reduce the thickness of protective layer, making thin-walled concrete floating structures possible. Finally, concrete floating structures are more prone to tensile stress compared to land structures, leading to concrete cracking. Significant rusting of the reinforcing steel happens, followed by localized concrete spalling and eventual structural failure. FRP reinforcement can improve the durability of concrete after cracking and avoid accelerated corrosion.

However, it should be noted that the low elastic modulus of FRP reinforcement will not improve the cracking load of concrete structure. Although the durability of structure after cracking is guaranteed, water seepage problem is still a great hidden danger for floating platform. Therefore, it is necessary to develop a specific structural form for FRP reinforced concrete floating structure. On the one hand, tensile stress in the floating structure needs to be reduced through special form. On the other hand, sealing function needs to be stripped from concrete structure to reduce the influence of concrete cracking.

Based on the above considerations, this paper proposes a novel bamboo-raft-type floating structure (BRT-FS) assembled by FRP reinforced concrete tubes, as shown in Fig. 1. The concept is a new very large floating structures (VLFS) type inspired from bamboo raft, a traditional Chinese transport. Longitudinal bamboos are replaced by concrete tubes and transverse bamboos are replaced by UHPC holding beams. Corrosion-resistant FRP composites are employed to improve structural life span. The structure adopts tubular section to form arch effect, diminishing the risk of transverse cracking. Prestressed CFRP plates are arranged inside to reduce the risk of longitudinal cracking. At the same time, foldable bellows are laid inside the tube to separate floating function from bearing function.

In this paper, the structure system and structure design are introduced first. In order to obtain the operation conditions of BRT-FS, the mechanical performance of BRT-FS is analyzed from two levels, which are hydroelastic analysis and structural analysis. According to the special characteristics of BRT-FS, a new finite element-boundary element (FE-BE) method is proposed based on Timoshenko beam element. Hydroelastic analysis is conducted under different wave directions, wave periods, water depths, and structural dimensions. For structural analysis, bending capacity is calculated and checked based on the structural response in hydroelastic analysis.

2. Structure system

BRT-FS is designed to be utilized in nearshore scenarios including tourism, marine aquaculture, photovoltaic power generation, and so on. The platform is anchored to the seafloor by dolphin-fender mooring system, which restricts the horizontal displacement of the structure while releasing the vertical displacement[33]. Due to the limitation of the mooring system, the expected water depth of structure is 10 – 30 m. The wave conditions applicable to the structure will be obtained by

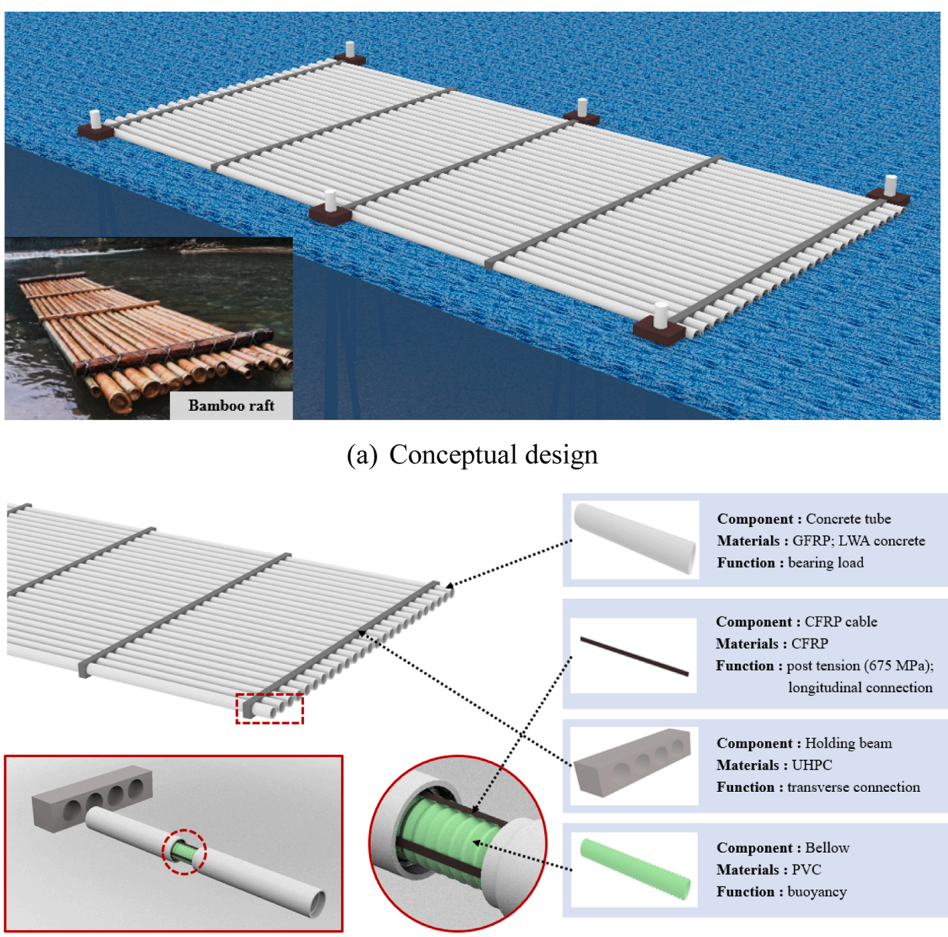

(b) Structural configuration illustration

Fig. 1. BRT-FS assembled by FRP reinforced concrete tubes.

hydroelastic analysis and structural analysis in the following sections.

As illustrated in Fig. 1(b), BRT-FS comprises four fundamental components: concrete tube, carbon fiber-reinforced polymer (CFRP) cable, holding beam, and bellow. Concrete tubes are connected in longitudinal direction with post-tensioned CFRP cables and transversely through holding beams. CFRP cables are prestressed to slow down cracking process and ease concrete tube assembly. After post-tension, the ends of short tubes are connected to form a long tube longitudinally, creating rigid tube-tube joints. In lateral direction, rows of concrete tubes are connected through holding beams. In this way, the lateral bending stiffness is obtained. Foldable bellows passing through concrete tubes create an enclosed area with buoyancy by sealing in suitable places.

Two size types are selected for personnel and vehicle applications. Mechanical properties of load-bearing components for both types are listed in Table 1. Moreover, different tube sizes can apply in one structure, realizing high transport efficiency by nesting placement. Note that for brevity, only personnel operation type is considered for further analysis in the paper. Considering personnel demand, the upper design load of the structure needs to exceed 4.5 kN/m^2. This parameter will influence the displacement and size of the structure.

3. Structure design

3.1. Concrete tube

The concrete tubes use glass fiber-reinforced polymer (GFRP) bars and lightweight aggregate concrete (LWAC) as raw materials. GFRP reinforced concrete has similar mechanical properties as normal reinforced concrete[9] but better corrosion resistance[2,4]. Besides, LWAC reduces 20 % the density of normal aggregate concrete, which is beneficial for floating platforms and other projects that are sensitive to structural weight. Concrete tube has a circular section rather than a square section. Advantages include the ability to create an arch effect to resist transverse cracking, the ability to be mass-produced by mandrel vibration, and the ability to obtain a larger cross-sectional area for the same material consumption.

Considering the actual displacement demand of the floating platform, an optimal section size analysis of concrete tubes is carried out to select the proper section dimension. The inner diameter and thickness are optimized to satisfy the topside load demand. In this design, the waterline is considered to be above the center of the concrete tube. A waterline near the tube centerline can increase the waterline area, inhibiting the heave of structure. However, a too close distance between the waterline and centerline will reduce the sturcture displacement. 3/4 of the outer diameter is selected as the maximum draft. The density of seawater is assumed to be 1020 kg/m^3. Considering transportation limitations and load requirements, an outer diameter of 2360 mm and a thickness of 180 mm are selected. In this condition, the maximum topside load is 4.76 kN/m^2. The concrete tube state under empty (minimum draft) and full topside loads (maximum draft) are shown in

Table 1
Mechanical properties of the load-bearing components: concrete tube, CFRP cable, and holding beam.

Components	Dimension		ρ (kg/m^3)	E (GPa)
	personnel operation	vehicle operation		
Concrete tube	inner diameter 2 m thickness 180 mm	inner diameter 3 m thickness 270 mm	2000	30
CFRP cable	100 mm × 5 mm (4)	100 mm × 5 mm (6)	1600	150
Holding beam	0.5 m × 3 m	0.75 m × 4.5 m	2500	40

* For brevity, only personnel operation type is considered for further analysis in the paper.

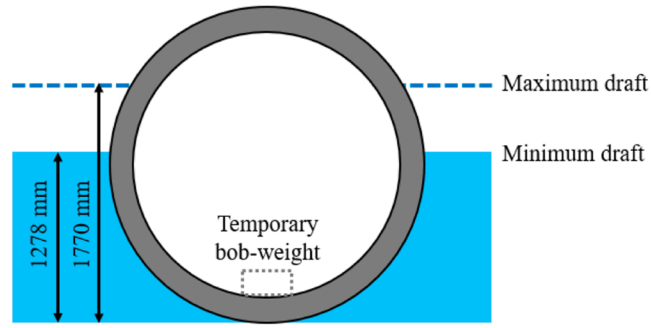

Fig. 2. State of concrete tube under empty (minimum draft) and full topside loads (maximum draft).

Fig. 2. Fig. 3 shows the reinforcement arrangement in a concrete tube. Longitudinal reinforcement is GFRP bars with a diameter of 28 mm. Because concrete tubes undertake bending in the vertical direction, the number of GFRP bars increases at both the top and bottom. Stirrups are 16 mm GFRP bars with intervals of 200 mm. To ease assembly, bob-weight can be added to the tube bottom to restrict the tube from rotation, then removed after assembly. Socket joints are applied to the end of these tubes, which are widely used in concrete drainage tubes.

3.2. CFRP cable

CFRP is a composite material with resin as matrix and carbon fiber as reinforcement. Compared with other FRP, CFRP has prominent characteristics of high strength and corrosion resistance[15]. Therefore, the application of CFRP has attracted increasing attention in ocean engineering[29,39]. As a common CFRP product, CFRP plate cable takes full advantage of high tensile strength and has been utilized as prestressed cable. However, the shear performance of CFRP is poor, making anchorage a crucial problem in its application[1]. Compared with circular section, plate section has higher anchoring efficiency due to the large perimeter-area ratio.

Each CFRP cable is prestressed to 675 MPa (approximately 30 % of the ultimate strength). To avoid damage in CFRP cables caused by external loads, these CFRP cables are arranged inside concrete tubes in circumferential distribution. The anchorage devices are fixed on the inner wall of concrete tubes for post-tensioning. Limited by the huge dimension of BRT-FS, CFRP cables are post-tensioned in sections, each containing two or three concrete tubes. CFRP plate anchorage devices are already a mature product on the market and will not be introduced here.

3.3. Holding beam

Holding beams are made from ultra-high performance concrete (UHPC) with a maximum strength of 200 MPa and better durability than conventional concrete[21]. There is no need to take into account the corrosion problem of UHPC in seawater because its chloride diffusion coefficient is orders of magnitude lower than that of conventional concrete. Holding beams have circle holes for concrete tubes crossing through. The interval of these holes is 2500 mm, leaving 140 mm interspace between concrete tubes. The high strength of UHPC is supposed to be adequate, which is not considered for the bearing capacity check in this paper.

3.4. Construction scheme

The construction of BRT-FS contains six main steps, as Fig. 4 shows:

1) Factory prefabrication. Precast production of concrete tubes and holding beams in a land factory;

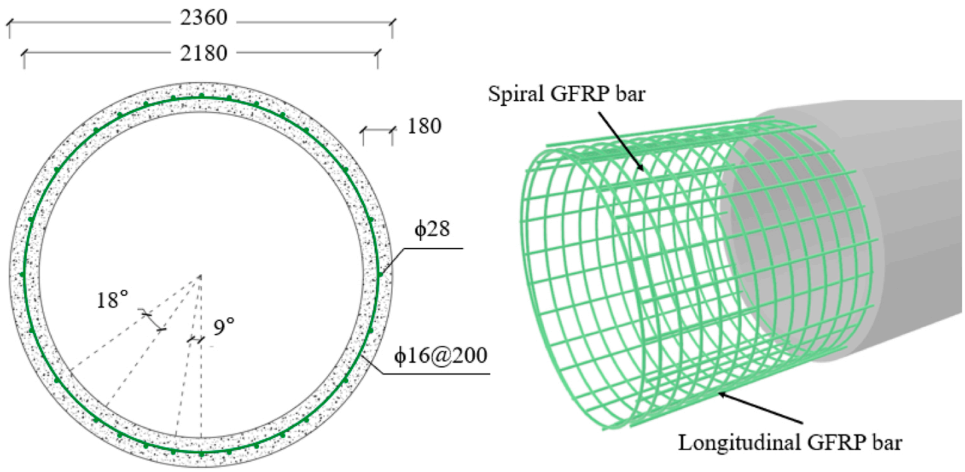

Fig. 3. GFRP reinforcement arrangement in a concrete tube (unit in mm).

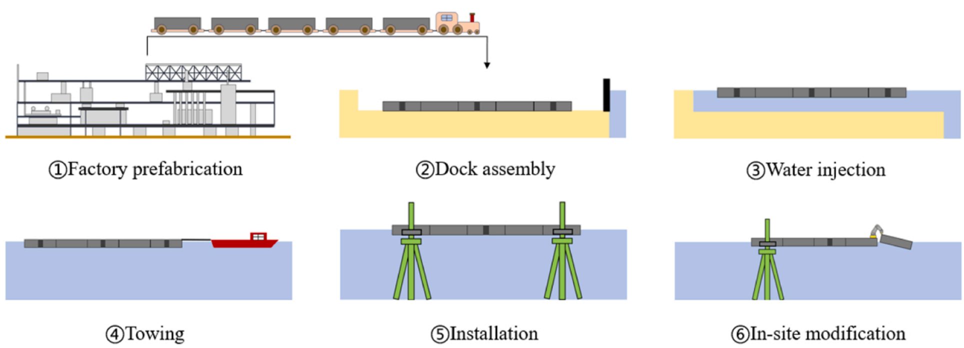

Fig. 4. Construction process of BRT-FS.

2) Dock assembly. Assemble BRT-FS in the dock;
3) Water injection. Inject water into dock to float the structure in seawater;
4) Towing. Tow the assembled module to the intended location;
5) Installation. Install the mooring system and fix it to several holding beams;
6) In-site modification. Repeat steps 1) −6) until the whole structure is completed.

The specific assembly process of BRT-FS is shown in Fig. 5. Firstly, holding beams are placed, which allows concrete tubes to cross through and be fixed into. The ends of the concrete tubes fixed to holding beams are connected by other concrete tubes. Note that, to avoid tube end connections lying in a row which may cause an apparent weakness in certain longitudinal sections, tube-tube joints are arranged in a stagger. Then in concrete tubes, CFRP cables pass through and post-tensioned, and bellows are unfolded. Cushion rubbers are installed at last to support topside modules.

4. Hydroelastic analysis by FE-BE method

4.1. Simplified model

The elasticity of VLFS results in the interaction of fluid field and

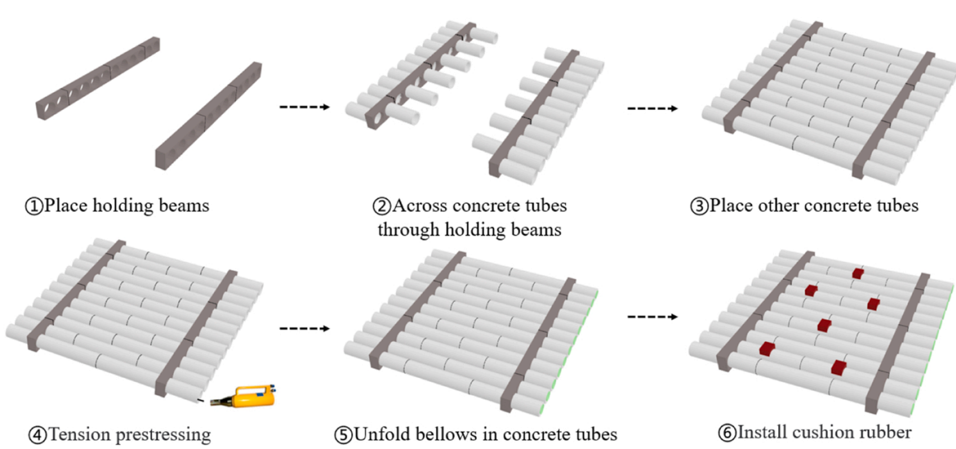

Fig. 5. Assembly process of BRT-FS.

structural deformation. For numerical investigation of the fluid-structure interaction, hydroelastic analysis is required. The state-of-the-art method for solving hydroelastic problem is finite element-boundary element (FE-BE) method[30]. To acquire the structural hydroelastic response including deflection and internal force, FE-BE method is employed in the frequency domain.

The assembled floating structure in water is simplified into the fluid-structure interaction problem as shown in Fig. 6. The structure consists of n tubes in the longitudinal direction and m rows of tubes in the transverse direction. The length of each tube is l. The diameter of each tube is D. The angle between incident wave direction and longitudinal direction is θ_w. The cracking of concrete tubes is suppressed under normal wave conditions. As a result, the mechanical properties of the concrete tubes are considered as linear elastic. The connection between dolphin-fender mooring system and structure is assumed to have vertical freedom and rotation freedom[26].

Seawater is assumed to be an ideal fluid, which is irrotational, incompressible, and non-viscous. The fluid domain is denoted as Ω, and the depth is H. It has no boundary in the x and y direction. The bottom surface ($z = -H$) is the seabed boundary (S_{SB}). The top surface ($z = 0$) is the free boundary (S_F) and the wetted surface of the structure (S_{HB}). S_∞ is the infinite boundary, as shown in Fig. 6(b) and Fig. 6(c). The amplitude of incident wave is A.

Most VLFS feature square cross-sections and can be simplified into Kirchhoff plate and Mindlin plate for hydroelastic analysis[19,26,31]. However, BRT-FS is comprised of cylindrical tubes, and each row of these tubes exhibits a large aspect ratio. In such cases, beam elements are more suitable for hydroelastic analysis than plate elements. Meanwhile, the large size of the concrete tube makes shear deformation and rotational inertia unreasonable to be ignored. As a result, the concrete tubes and holding beams are regarded as Timoshenko beam elements to facilitate calculation, as shown in Fig. 7. For the convenience of hydroelastic analysis, the structural system needs to be transformed into simple geometry. The influence of CFRP cable on the stiffness of concrete tube before cracking is negligible. Structural attachments such as CFRP cables, holding beams, and bellows have low mass ratio and limited dynamic influence on concrete. Hence, only the motion response of concrete tube and holding beam is considered in the analysis of structural motion. For concrete tube element, it has one translational degree of freedom (TDOF) of w_z and one rotational degree of freedom (RDOF) of θ_y. For holding beam element, it has one TDOF of w_z and one RDOF of θ_x.

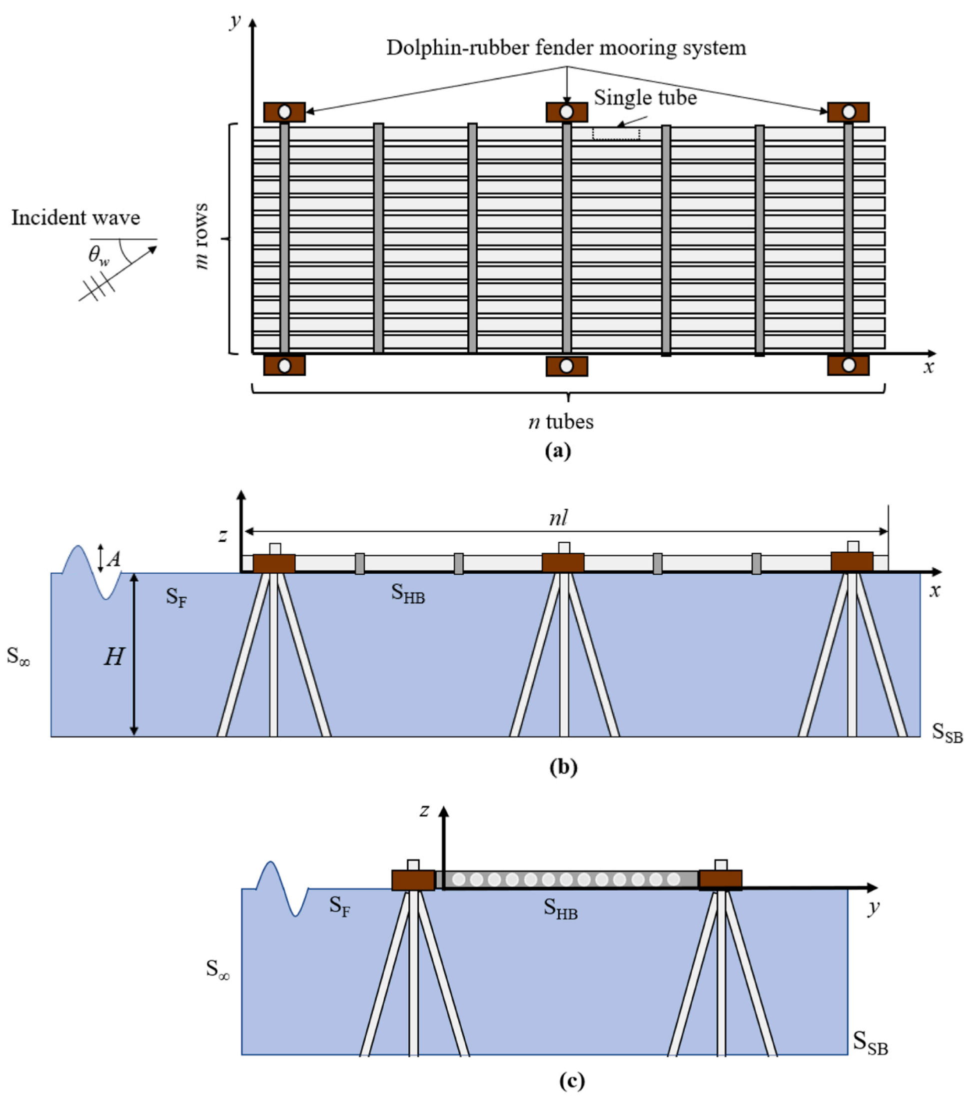

Fig. 6. Schematic diagram of coupled fluid-structure problem: (a) top view; (b) front view; (c) side view.

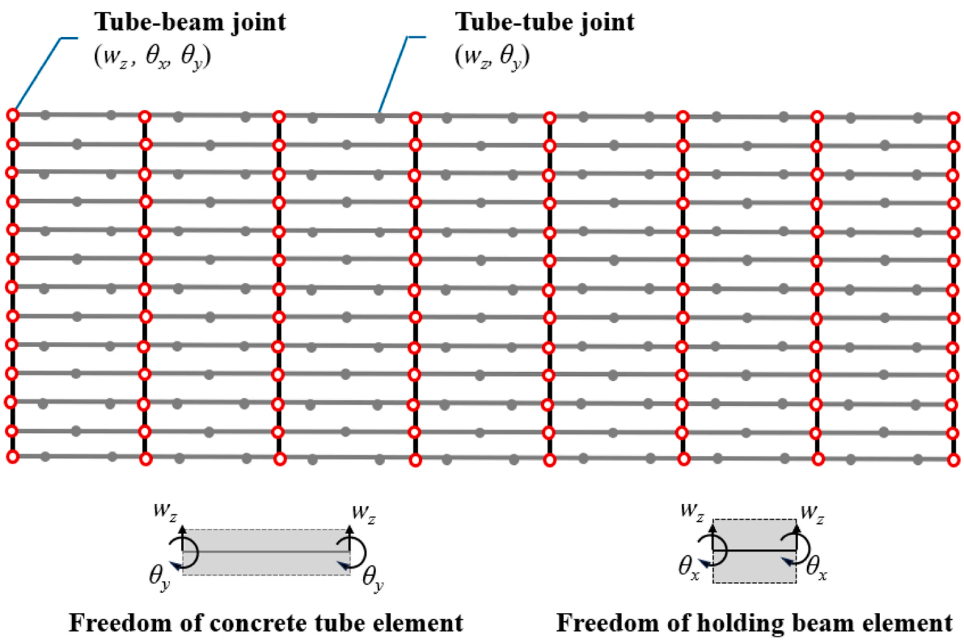

Fig. 7. Simplified structural model of BRT-FS.

The simplified model has two types of joints, tube-tube joint and tube-beam joint. Under normal wave conditions, tube-tube joints are designed not to generate relative rotation, treated as rigid connections. This implies that tube-tube joint has one TDOF and one RDOF. The situation for tube-beam joints is more complicated. The different bending directions of concrete tube and holding beam provide tube-beam joint with one TDOF and two RDOF. Since concrete tubes can rotate freely within the holding beam, the bending of the holding beam will not induce torsion in the concrete tube. Nevertheless, variations in the rotation of different rows of concrete tubes can result in torsion of the holding beams. Twisting spring is utilized to replace the torsional stiffness of holding beam, as shown in Fig. 8. The additional bending moment acting on the joint satisfies Eqs. (1) and (2):

$$\overline{M}_{x,ij} = -G_h K_h(\theta_{x,i} - \theta_{x,j})/L_h \tag{1}$$

$$\overline{M}_{x,ji} = -G_h K_h(\theta_{x,j} - \theta_{x,i})/L_h \tag{2}$$

where $\overline{M}_{x,ij}$ is the additional bending moment acting on joint i for the twisting spring between joint i and j, which is the same rule for $\overline{M}_{x,ji}$. $\theta_{x,i}$ and $\theta_{x,j}$ are the RDOF in x direction of joint i and j, respectively. G_h is the shear modulus of holding beam. L_h is the interval between concrete tubes. K_h is the equivalent polar moment of inertia of holding beam. For rectangular solid section, K_h is acquired from Eq. (3).

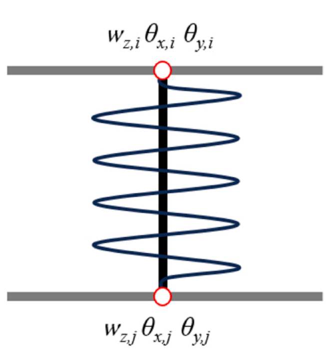

Fig. 8. Tube-beam joint details between joint i and joint j.

$$K_h = d_h {b_h}^3\left[\frac{1}{3} - 0.21\frac{b_h}{d_h}\left(1 - \frac{(b_h/d_h)^4}{12}\right)\right] \tag{3}$$

where d_h and b_h are the depth and width of holding beam cross-section.

4.2. Hydroelastic analysis methodology

4.2.1. Variational equation for plate motion

According to Timoshenko beam theory, the beam motion is described by the vertical displacement w and rotation θ. Shear deformation and rotational inertia are considered compared to Euler-Bernoulli beam theory. Under shear force, the section perpendicular to the neutral axis is no longer perpendicular after deformation. In the local coordinate system x, y, and z axes represent the length, width, and thickness directions of the element, respectively. Denoting ε and γ as axial and shear strains at the intersection point of cross section and neutral axis, which are [35]:

$$\varepsilon = -z\frac{\mathrm{d}\theta}{\mathrm{d}x} \tag{4}$$

$$\gamma = -\theta + \frac{\mathrm{d}w}{\mathrm{d}x} \tag{5}$$

The structure under free boundary condition needs to satisfy the constraint condition that both bending moment and shear force vanish at edges, which means:

$$M = EI\frac{\mathrm{d}\theta}{\mathrm{d}x} = 0 \tag{6}$$

$$Q = \frac{G_c A_c}{\kappa}\gamma = 0 \tag{7}$$

where elastic modulus E, moment of inertia I, and cross-sectional area A_c are defined. G_c and κ are the shear modulus and shear correction factor (6/5 for rectangular section and 10/9 for circle section), respectively. Both concrete tubes and holding beams apply this constitutive equation.

The dynamic equations can be derived from the principle of minimum potential energy. The potential energy U concludes bending strain energy, shear strain energy, work done by twisting spring, and work done by fluid pressure in vertical direction, as shown in Eq. (8). The kinetic energy T concludes vertical kinetic energy and rotational kinetic energy, as shown in Eq. (9).

$$U=\frac{1}{2}\int_{S_{HB}}\int_0^h \varepsilon E\varepsilon \mathrm{d}z\mathbf{dx}+\frac{1}{2}\int_{S_{HB}}\int_0^h \gamma\frac{G_c}{\kappa}\gamma \mathrm{d}z\mathbf{dx}-\frac{1}{2}\sum\left(M_{x,ij}\theta_{x,i}+M_{x,ji}\theta_{x,j}\right)-\int_{S_{HB}} p_z w\mathbf{dx} \tag{8}$$

$$T=\frac{1}{2}\int_{S_{HB}}\left(\frac{\partial^2 w}{\partial t^2}\right)\rho A_c\frac{\partial^2 w}{\partial t^2}\mathbf{dx}+\frac{1}{2}\int_{S_{HB}}\left(\frac{\partial^2\theta}{\partial t^2}\right)\rho I\frac{\partial^2\theta}{\partial t^2}\mathrm{d}x \tag{9}$$

where $\mathbf{dx}$ means integral in both longitudinal and transverse directions, while dx means only integral in longitudinal direction. As the bottom of the concrete tube is cambered instead of flat, the direction of fluid pressure $p(x, y)$ deviates from the z direction. The transverse component of p is much smaller than the vertical component, and its impact on the vertical motion is neglected. Only the influence of the vertical component p_z on the structure is taken into consideration. p_z and p adhere to the relationship depicted in Eq. (10). $\varphi(x, y)$ is the angle between water pressure and vertical direction. In Eq. (11), p can be calculated according to Bernoulli's equation.

$$p_z = p\cos\varphi \tag{10}$$

$$p=-\rho_w\left(\frac{\partial\phi}{\partial t}+gw\right)=i\omega\rho_w\phi-\rho_w gw \tag{11}$$

where ρ_w is the fluid density, g is the gravitational acceleration, and $\phi(x, y)$ is the velocity potential of the fluid at the interface between structure and fluid (S_{HB}).

According to Hamilton's principle, the following equation (after omitting the time factor $e^{-i\omega t}$) is obtained from Eqs. (1), (2), and (8) - (11). The fluid pressure can be decomposed into two parts: hydrodynamic pressure and hydrostatic pressure.

$$\begin{aligned}&\int_{S_{HB}}\int_0^h \delta\varepsilon E\varepsilon \mathrm{d}z\mathbf{dx}+\int_{S_{HB}}\int_0^h \delta\gamma\frac{G_c}{\kappa}\gamma \mathrm{d}z\mathbf{dx}-\omega^2\int_{S_{HB}}\delta w\rho A_c w\mathrm{d}x-\omega^2\int_{S_{HB}}\delta\theta\rho I\theta \mathrm{d}x\\&=-\sum\delta\left(\theta_{x,i}-\theta_{x,j}\right)\frac{G_hK_h}{L_h}\left(\theta_{x,i}-\theta_{x,j}\right)+i\omega\rho_w\int_{S_{HB}}\delta w\phi\cos\varphi\mathbf{dx}-\rho_w g\int_{S_{HB}}\delta w\cos\varphi w\mathbf{dx}\end{aligned} \tag{12}$$

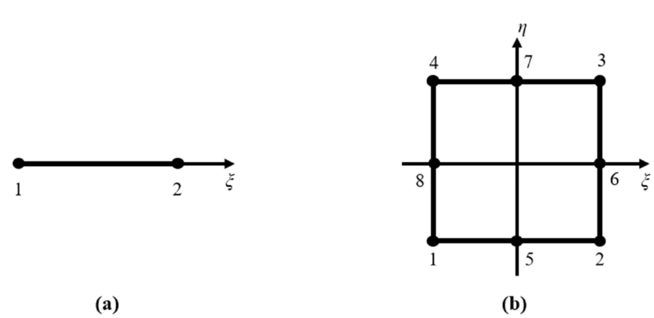

Fig. 9. Isoparameteric elements for structures: (a) beam element; (b) quadratic-serendipity plane element.

4.2.2. Discretization of motion equation by FEM

Finite element method (FEM) is a common method for elastic mechanics. It can transform the structural integral equation into the form of global matrix. The primary structural components experience bending moment and shear force, yet the distribution of vertical fluid action across the width of these components is non-uniform. So beam elements are employed to analyze the deformation and dynamic response, while plane elements are used to consider the vertical fluid action. Beam element contains 2 nodes. Since only a single element is used to calculate fluid action in the concrete tube width direction, a quadratic-serendipity plane element with 8 nodes is adopted for better accuracy. The isoparameteric elements for these two types are shown in Fig. 9.

For each beam element, the displacement field is$\mathbf{w}_b=\left[w_b\quad\theta_b\right]^{\mathrm{T}}$, potential field is$\boldsymbol{\phi}_b=\left[\phi_b\quad 0\right]^{\mathrm{T}}$. In order to maintain the continuity of displacement and rotation, linear interpolation is used for shape function. The values inside the element can be obtained from the shape function and node values:

$$\mathbf{w}_b=\mathbf{N}_b\widehat{\mathbf{w}}_b \tag{13}$$

$$\boldsymbol{\phi}_b=\mathbf{N}_b\widehat{\boldsymbol{\phi}}_b \tag{14}$$

where $\widehat{\mathbf{w}}_b=\left[w_{b1}\quad\theta_{b1}\quad w_{b2}\quad\theta_{b2}\right]^{\mathrm{T}}$ is the nodal displacement vector and $\widehat{\boldsymbol{\phi}}_b=\left[\phi_{b1}\quad 0\quad\phi_{b2}\quad 0\right]^{\mathrm{T}}$ is the nodal velocity potential vector. $\mathbf{N}_b$is the shape function:

$$\mathbf{N}_b=\begin{bmatrix}N_{b1} & 0 & N_{b2} & 0\\ 0 & N_{b1} & 0 & N_{b2}\end{bmatrix}^{\mathrm{T}} \tag{15}$$

where $N_{b1}=(1-\xi)/2$and $N_{b2}=(1+\xi)/2$.

For each plane element, the displacement field is$\mathbf{w}_p=\left[w_p\quad\theta_p\right]^{\mathrm{T}}$, potential field is$\boldsymbol{\phi}_p=\left[\phi_p\quad 0\right]^{\mathrm{T}}$. Similar to beam element, the values inside the element can be obtained from the shape function and node values:

$$\mathbf{w}_p=\mathbf{N}_p\widehat{\mathbf{w}}_p \tag{16}$$

$$\boldsymbol{\phi}_p=\mathbf{N}_p\widehat{\boldsymbol{\phi}}_p \tag{17}$$

where $\widehat{\mathbf{w}}_p=\left[w_{p1}\quad\theta_{p1}\quad\cdots\quad w_{p8}\quad\theta_{p8}\right]^{\mathrm{T}}$ is the nodal displacement vector and $\widehat{\boldsymbol{\phi}}_p=\left[\phi_{p1}\quad 0\quad\cdots\quad\phi_{p8}\quad 0\right]^{\mathrm{T}}$ is the nodal velocity potential vector. $\mathbf{N}_p$is the shape function:

$$\mathbf{N}_p=\begin{bmatrix}N_{p1} & 0 & \cdots & N_{p8} & 0\\ 0 & N_{p1} & & 0 & N_{p8}\end{bmatrix}^{\mathrm{T}} \tag{18}$$

where

$$N_{pj} = \frac{1}{4}(1+\xi_j\xi)(1+\eta_j\eta)(\xi_j\xi+\eta_j\eta-1) \text{ for corner nodes } j=1,2,3,4 \tag{19}$$

$$N_{pj} = \frac{1}{2}(1-\xi^2)(1+\eta_j\eta) \text{ for mid}-\text{side nodes } j=5,7 \tag{20}$$

$$N_{pj} = \frac{1}{2}(1+\xi_j\xi)(1-\eta^2) \text{ for mid}-\text{side nodes } j=6,8 \tag{21}$$

To calculate elements with different nodes in the coupling equation, the following relationship is established:

$$\widehat{\mathbf{w}}_p = \mathbf{T}\widehat{\mathbf{w}}_b \tag{22}$$

$$\widehat{\boldsymbol{\phi}}_p = \mathbf{T}\widehat{\boldsymbol{\phi}}_b \tag{23}$$

$$\mathbf{T} = \begin{bmatrix} \mathbf{I} & 0 & 0 & \mathbf{I} & \frac{1}{2}\mathbf{I} & 0 & \frac{1}{2}\mathbf{I} & \mathbf{I} \\ 0 & \mathbf{I} & \mathbf{I} & 0 & \frac{1}{2}\mathbf{I} & \mathbf{I} & \frac{1}{2}\mathbf{I} & 0 \end{bmatrix}^{\mathrm{T}} \left(\mathbf{I} = \begin{bmatrix} 1 & 0 \\ 0 & 1 \end{bmatrix}\right) \tag{24}$$

The relationship means velocity potential and displacement is the same in cross-section. The value on mid-side point is the average of the corner point values. The matrices for beam element and plane element have the same dimension through the transformation matrix **T**.

$$\mathbf{M}_d = \int_{\triangle d} \mathbf{N}_b^{\mathrm{T}}\mathbf{m}\mathbf{N}_b \mathrm{d}x \tag{28}$$

$$\mathbf{R}_d = \int_{\triangle d} \mathbf{N}_b^{\mathrm{T}}\mathbf{r}\mathbf{N}_b \mathrm{d}x \tag{29}$$

$$\mathbf{K}_{\mathrm{I}zd} = \int_{\triangle d} \mathbf{T}^{\mathrm{T}}\mathbf{N}_p^{\mathrm{T}}\mathbf{k}_{\mathrm{I}z}\mathbf{N}_p\mathbf{T}\mathrm{d}\mathbf{x} \tag{30}$$

$$\mathbf{K}_{rfd} = \int_{\triangle d} \mathbf{T}^{\mathrm{T}}\mathbf{N}_p^{\mathrm{T}}\mathbf{k}_{rf}\mathbf{N}_p\mathbf{T}\mathrm{d}\mathbf{x} \tag{31}$$

where $\mathbf{K}_{fd}$, $\mathbf{K}_{sd}$, $\mathbf{M}_d$, $\mathbf{R}_d$, $\mathbf{K}_{\mathrm{I}zd}$, $\mathbf{K}_{rfd}$ are respectively element bending, shear, mass, rotational inertia, vertical unit, and restoring force matrices. Δd is the element domain. The matrix $\mathbf{m}$, $\mathbf{r}$, $\mathbf{k}_{\mathrm{I}z}$, and $\mathbf{k}_{rf}$ are respectively:

$$\mathbf{m} = \begin{bmatrix} \rho A_c & 0 \\ 0 & 0 \end{bmatrix}, \mathbf{r} = \begin{bmatrix} 0 & 0 \\ 0 & \rho I \end{bmatrix}, \mathbf{k}_{\mathrm{I}z} = \begin{bmatrix} \cos\varphi & 0 \\ 0 & \cos\varphi \end{bmatrix}, \mathbf{k}_{rf} = \begin{bmatrix} \rho_w g\cos\varphi & 0 \\ 0 & 0 \end{bmatrix} \tag{32}$$

where φ is the angle between fluid pressure and vertical direction.

The global twisting string matrix $\mathbf{K}_m$ is the sum of all the local twisting string matrix, which is:

$$\mathbf{K}_{md} = \frac{G_h K_h}{L_h} \begin{array}{c|cccc} & \cdots & i & & j \\ i & & 1 & & -1 \\ & & & \cdots & \\ j & & -1 & & 1 \\ & & & & \cdots \end{array} (\text{twisting string between joint } i \text{ and joint } j) \tag{33}$$

Minimizing Eq. (12) with respect to $\widehat{\mathbf{w}}$, and integrating element matrix into global matrix, the motion equation of the structure can be written as:

$$(\mathbf{K}_f + \mathbf{K}_s + -\omega^2\mathbf{M} - \omega^2\mathbf{R})\widehat{\mathbf{w}} = -\mathbf{K}_m\widehat{\mathbf{w}} + i\omega\rho_w\mathbf{K}_{\mathrm{I}z}\widehat{\boldsymbol{\phi}} - \mathbf{K}_{rf}\widehat{\mathbf{w}} \tag{25}$$

where $\widehat{\mathbf{w}}$ and $\widehat{\boldsymbol{\phi}}$ are the global vectors of the nodal displacement and velocity potential. $\mathbf{K}_f$ and $\mathbf{K}_s$ are the global bending and shear stiffness matrices using reduced integration; while $\mathbf{M}$, $\mathbf{R}$, $\mathbf{K}_{\mathrm{I}z}$, and $\mathbf{K}_{rf}$ are the global mass, rotational inertia, vertical unit, and restoring force matrices, respectively. Each global matrix is assembled by the following element matrix using finite element method (calculation procedure for $\mathbf{K}_{fd}$ and $\mathbf{K}_{sd}$ referring to [25]):

$$\mathbf{K}_{fd} = \frac{EI}{l_d}\begin{bmatrix} 0 & 0 & 0 & 0 \\ 0 & 1 & 0 & -1 \\ 0 & 0 & 0 & 0 \\ 0 & -1 & 0 & 1 \end{bmatrix} \tag{26}$$

$$\mathbf{K}_{sd} = \frac{GA_c}{4\kappa l_d}\begin{bmatrix} 4 & 2l & -4 & 2l \\ 2l & l^2 & -2l & l^2 \\ -4 & -2l & 4 & -2l \\ 2l & l^2 & -2l & l^2 \end{bmatrix} \tag{27}$$

$$\mathbf{K}_m = \sum \mathbf{K}_{md} \tag{34}$$

The numerical integration for Eqs. (28) - (31) is conducted based on Gauss-Legendre equation. $\mathbf{M}_d$ and $\mathbf{R}_d$ are calculated through two Gaussian points in beam element. $\mathbf{K}_{\mathrm{I}zd}$ and $\mathbf{K}_{rf}$ are calculated through nine Gaussian points in plane element.

4.2.3. Solution for fluid velocity potential

Boundary element method (BEM) is a common method for solving fluid problem. The linear wave hypothesis is adopted, which means the wave height is very small relative to the wavelength and water depth. The fluid velocity potential satisfies the Laplace equation:

$$\nabla^2\phi(x,y,z) = 0 \text{ in fluid domain } \Omega \tag{35}$$

The boundary conditions of the fluid domain are:

$$\frac{\partial\phi}{\partial z}(x,y,0) = -i\omega w(x,y) \text{ on the wetted surface } \mathrm{S_{HB}} \tag{36}$$

$$\frac{\partial\phi}{\partial z}(x,y,0) = \frac{\omega^2}{g}\phi(x,y,0) \text{ on the free boundary } \mathrm{S_F} \tag{37}$$

$$\frac{\partial \phi}{\partial z}(x, y, -H) = 0 \text{ on the seabed boundary } S_{SB} \tag{38}$$

$$\lim_{|\mathbf{x}| \to \infty} \sqrt{|\mathbf{x}|} \left(\frac{\partial(\phi - \phi^{in})}{\partial |\mathbf{x}|} - ik(\phi - \phi^{in}) \right) = 0 \text{ on the infinite boundary } S_\infty \tag{39}$$

where S_{HB}, S_F, S_{SB}, and S_∞ are defined in Fig. 6 and Section 4.1; $\mathbf{x} = (x, y)$ is the coordinate of fluid particle in Ω; ω and k represent the wave frequecy and wave number satisfying the dispersion equation:

$$k \tanh kH = \frac{\omega^2}{g} \tag{40}$$

$\phi^{in}$is the velocity potential of the incident wave, calculated by the following equation[31]:

$$\phi^{in} = \frac{gA}{\omega} \frac{\cosh k(z+H)}{\cos kH} e^{ik(x \cos \theta_w + y \sin \theta_w)} \tag{41}$$

where A is half of the wave height and H is the depth of fluid domain Ω; while z is the thickness direction of the structure as shown in Fig. 6.

By substituting the boundary conditions (Eqs. (36) - (39)) into Laplace's equation (Eq. (35)) using Green's function, the velocity potential can be expressed as [26]:

$$\phi(\mathbf{x}_s) = \phi^{in}(\mathbf{x}_s) + \int_{S_{HB}} G\left(\mathbf{x}_s, \boldsymbol{\xi}\right) \left[\frac{\omega^2}{g} \phi(\boldsymbol{\xi}) + i\omega w(\boldsymbol{\xi}) \right] d\boldsymbol{\xi} \tag{42}$$

where $\mathbf{x}_s = (x, y)$ and $\boldsymbol{\xi} = (\xi, \eta)$ is the source point and field point. G is the Green function satisfying the boundary conditions, which is calculated according to the following equation[23]:

$$G\left(\mathbf{x}, \boldsymbol{\xi}\right) = -\sum_{r=0}^{\infty} \frac{K_0(k_r R)}{\pi H \left(1 + \frac{\sin 2k_r H}{2k_r H}\right)} \cos^2 k_r H \tag{43}$$

where k_r $(r \geq 1)$ is positive and satisfies the equation $k_r \tan(k_r H) = -\omega^2/g$. And $k_0 = -ik$ where k is the positive root of $k_r \tanh(k_r H) = \omega^2/g$. R is the distance between source point $\mathbf{x}$ and field point $\boldsymbol{\xi}$. K_0 is the modified Bessel function of the second kind.

The same quadratic-serendipity plane elements with fluid action are adopted in BEM. For the element domain, Eq. (42) can be discretized to:

$$\mathbf{K}_{Id} \widehat{\boldsymbol{\phi}}_p = \mathbf{K}_{Id} \widehat{\boldsymbol{\phi}}_p^{\text{in}} + \frac{\omega^2}{g} \sum_{e=1}^{n_n} \mathbf{g}_{pe} \widehat{\boldsymbol{\phi}}_e + i\omega \sum_{e=1}^{n_n} \mathbf{g}_{pe} \widehat{\mathbf{w}}_e \tag{44}$$

where $\widehat{\boldsymbol{\phi}}_p^{\text{in}}$ is nodal velocity potential vector of incident wave and $\mathbf{g}_{pe}$ is element Green function matrix (calculation procedure for $\mathbf{g}_{pe}$ referring to [34]). Eqs. (22) and (23) are adopted to convert plane element to beam element:

$$\mathbf{T}^{\mathrm{T}} \mathbf{K}_{Id} \mathbf{T} \widehat{\boldsymbol{\phi}}_b = \mathbf{T}^{\mathrm{T}} \mathbf{K}_{Id} \mathbf{T} \widehat{\boldsymbol{\phi}}_b^{\text{in}} + \frac{\omega^2}{g} \sum_{e=1}^{n_n} \mathbf{T}^{\mathrm{T}} \mathbf{g}_{pe} \mathbf{T} \widehat{\boldsymbol{\phi}}_{be} + i\omega \sum_{e=1}^{n_n} \mathbf{T}^{\mathrm{T}} \mathbf{g}_{pe} \mathbf{T} \widehat{\mathbf{w}}_{be} \tag{45}$$

where $\mathbf{K}_{Id}$ is the element unit matrix, which is similar to $\mathbf{K}_{Izd}$:

$$\mathbf{K}_{Id} = \int_{\triangle d} \mathbf{N}_p^{\mathrm{T}} \mathbf{k}_I \mathbf{N}_p \mathrm{d}x \tag{46}$$

$$\mathbf{k}_I = \begin{bmatrix} 1 & 0 \\ 0 & 1 \end{bmatrix} \tag{47}$$

Integrating all n_n element matrices into the global matrix, we can get:

$$\mathbf{K}_I \widehat{\boldsymbol{\phi}} = \mathbf{K}_I \widehat{\boldsymbol{\phi}}^{in} + \frac{\omega^2}{g} \mathbf{G} \widehat{\boldsymbol{\phi}} + i\omega \mathbf{G} \widehat{\mathbf{w}} \tag{48}$$

where $\widehat{\boldsymbol{\phi}}^{in}$is the global nodal velocity potential vector of incident wave, $\mathbf{K}_I$ is the global unit matrix, and $\mathbf{G}$ is the global Green function matrix.

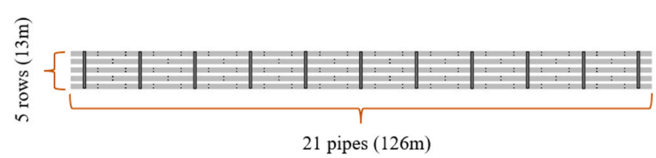

Fig. 11. A case study for BRT-FS.

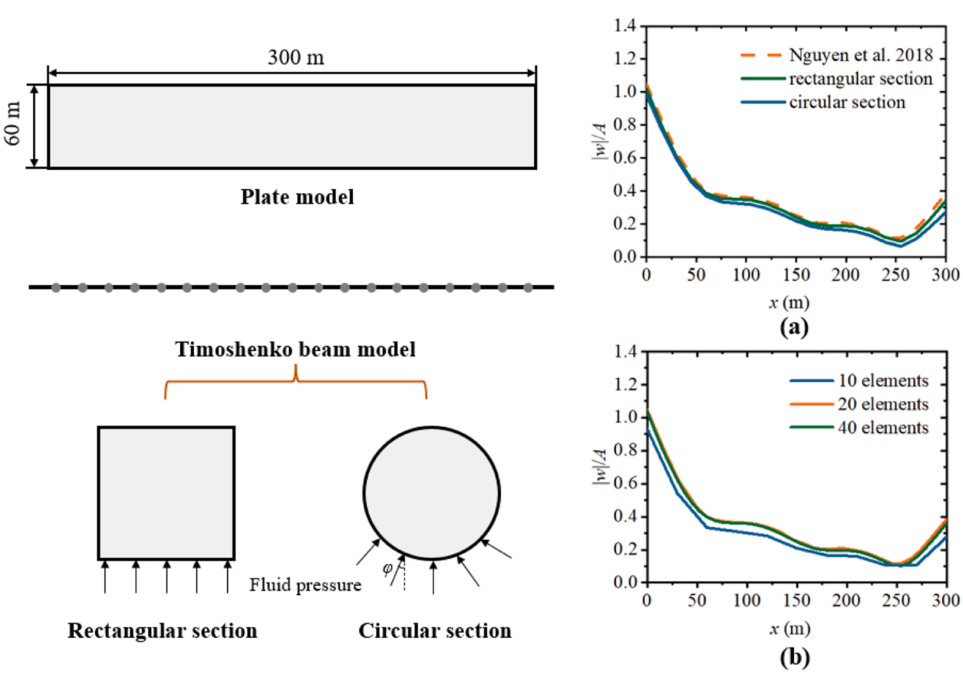

Fig. 10. Simplified validation model of a plate structure subjected to a longitudinal incident wave: (a) comparison between Mindlin plate model and Timoshenko beam model; (b) convergence results.

4.2.4. FE-BE solution method

Finite element-boundary element (FE-BE) method combines the advantages of finite element analysis and boundary element analysis, so it is suitable for solving fluid-structure interaction problems. The structure equation Eq. (25) and fluid motion equation Eq. (48) can be combined to:

$$\left(\mathbf{K}_f+\mathbf{K}_s+-\omega^2\mathbf{M}-\omega^2\mathbf{I}+\mathbf{K}_m+\mathbf{K}_{rf}+\omega^2\rho_w\mathbf{K}_{\mathrm{Iz}}\left(\mathbf{K}_{\mathrm{I}}-\frac{\omega^2}{g}\mathbf{G}\right)^{-1}\mathbf{G}\right)\widehat{\mathbf{w}}$$
$$=i\omega\rho_w\mathbf{K}_{\mathrm{Iz}}\left(\mathbf{K}_{\mathrm{I}}-\frac{\omega^2}{g}\mathbf{G}\right)^{-1}\mathbf{K}_{\mathrm{I}}\widehat{\boldsymbol{\phi}}^{in} \tag{49}$$

The nodal displacement vector $\widehat{\mathbf{w}}$ is obtained by solving the above equation. Element nodal moment $\mathbf{F}_{Md}$ can be calculated through element bending stiffness matrix as Eq. (50) shows. If the same node exists in different elements, average value is taken as the nodal moment at that node.

$$\mathbf{F}_{Md}=\mathbf{K}_{fd}\mathbf{w}_d \tag{50}$$

4.3. Model validation

It is necessary to compare the novel hydroelastic model described in this paper to the existing hydroelastic model. However, the majority of the existing hydroelastic models are based on rectangular sections. As a result, validation for both rectangular and circular section will be conducted. For rectangular section, the objective is to confirm the reliability of the transformation matrix **T**. While for circular section, the objective is to compare the differences between rectangular and circular section. Notably, rectangular section and circular section are set to have the same density, width, cross-section area, and moment of inertia, which is not possible in reality.

The validation model is a floating plate with a dimension of 300 m * 60 m * 2 m[26]. The incident wave in the longitudinal direction has a wavelength of 150 m. The water depth is 20 m. Material elastic modulus of the platform is 11.9 GPa with a density of 256.25 kg/m^3. The thickness-to-incident wavelength ratio is 0.0133, which satisfies thick plate assumption[17]. Fig. 10 illustrates the simplified process for the validation model. Because the lateral influence of head sea on the structure is negligible, the floating plate is simplified to Timoshenko beam with a smaller width to make the section closer to circular. For rectangular section, set φ as zero on the wetted surface. Mesh number for the longitudinal direction are 20. After meshing, the structure is analyzed by aforementioned FE-BE approach to solve the hydroelastic response.

The comparison between Mindlin plate model and Timoshenko beam model with rectangular and circular section is shown in Fig. 10 (a). The result indicates that the transformation matrix **T** is reliable and the influence of circular shape is relatively small. Meanwhile, a convergence test is further conducted on the model. Analysis results under various mesh number ranging from 10 - 40 are shown in Fig. 10 (b), which proves the convergence of the model.

4.4. Hydroelastic analysis of BRT-FS

4.4.1. A typical case study for hydroelastic analysis

In this section, a case study of hydroelastic analysis for BRT-FS is

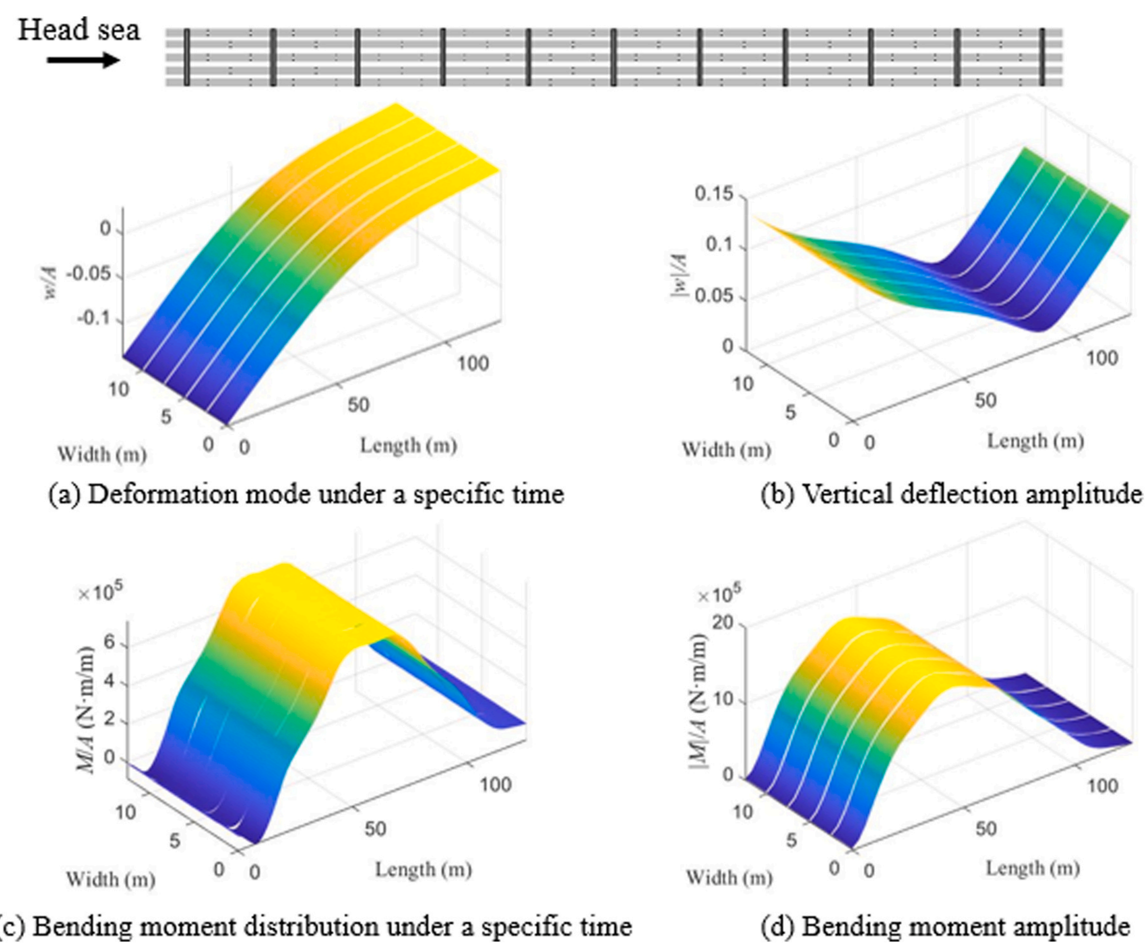

Fig. 12. Hydroelastic responses of assembled floating structure in a unit head sea: (a) and (b) vertical deflection; (c) and (d) bending moment response.

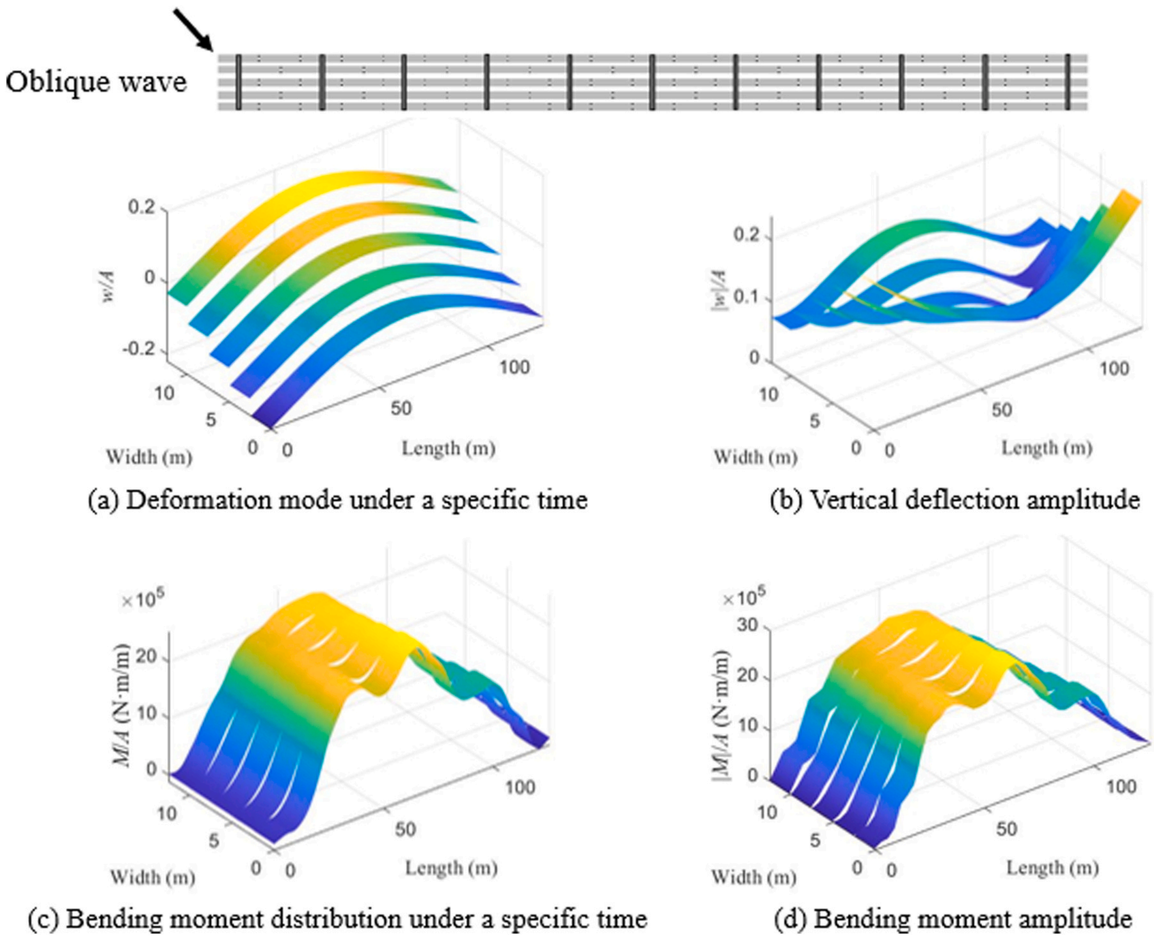

Fig. 13. Hydroelastic responses of assembled floating structure in a unit oblique wave: (a) and (b) vertical deflection; (c) and (d) bending moment response.

investigated. The structure has five rows of tubes joined by holding beams in the transverse direction, with a length of 126 m and a width of 13 m, as illustrated in Fig. 11. Holding beams are installed every two concrete tubes. Each row has 21 tubes of 6 m connected in the longitudinal direction. In Section 2, the design condition of the structure is given in a wide range. A typical wave condition will be selected for analysis in the case study. The influence of wave condition changes on the structural response will be described in the following sections. The typical wave condition has water depth H of 15 m and wave period T of 4 s. Corresponding to the incident-wave period, the wavelength-structural length ratio is 0.20, which means elastic effect on the structural response is remarkable.

The hydroelastic response of the proposed structure is analyzed by the novel hydroelastic model. The influences of GFRP reinforcement bars and CFRP cables on stiffness and density of concrete tubes are ignored. The average density of holding beams is calculated by the total mass without hole mass dividing total volume, which is 1042 kg/m^3. However, the average elastic modulus of holding beams is assumed to be the modulus of UHPC, because the tube-beam joints can enhance the stiffness. Other component property parameters refer to Table 1.

4.4.2. Influence of wave direction

Firstly, the hydroelastic response under a unit amplitude of head sea (wave incident direction is the longitudinal direction) is analyzed. The deformation mode of the platform under a specific time (zero phase angle) is indicated in Fig. 12 (a). The y axis is vertical deflection normalized by the wave amplitude A. For each node, take the maximum value during one period as the amplitude. The normalized vertical deflection amplitude is shown in Fig. 12 (b). The vertical deflection is smallest in the middle of structure, increasing linearly until reaching the peak value above 0.1 at both ends. Similarly, Fig. 12 (c) and Fig. 12 (d) show the bending moment distribution at zero phase angle and the normalized bending moment amplitude. There is almost no bending moment at the end of structure in the absence of constraint. A peak bending moment amplitude of 1.6×10^6 N·m/m occurs in the middle of structure, which is the weak area under head sea.

The same method is adopted to calculate the hydroelastic response under the unit oblique wave (the angle between the wave incident direction and longitudinal direction is 45°) and the unit beam sea (the wave incident direction is the transverse direction), as shown in Fig. 13 and Fig. 14. Under oblique wave, the hydroelastic response is quite complex. Different rows tend to exhibit different deformation patterns without holding beam constraints. However, holding beams limit the relative displacement and rotation between different rows. Different rows are forced to exhibit approximate deformation patterns. The maximum vertical deflection response exceeds that in the head sea, reaching 0.238. The moment response amplitude is larger within the third to seventh holding beams, with a peak value of 2.6×10^6 N·m/m, which is greater than that under head sea.

Under beam sea, the dimension along the wavelength direction decreases and the deflection response of the structure increases significantly. The deflections of the same concrete tube row are consistent and the structure remains almost planar at zero phase, indicating a small elastic deformation in this case. It is worth mentioning that in Fig. 13 (a) and (b) the structure appears to be "separated" as a result of significant displacement disparities among different rows. This is due to the fact that the deflection and dimension values are not in the same amplitude and the actual structure does not have such a significant deflection

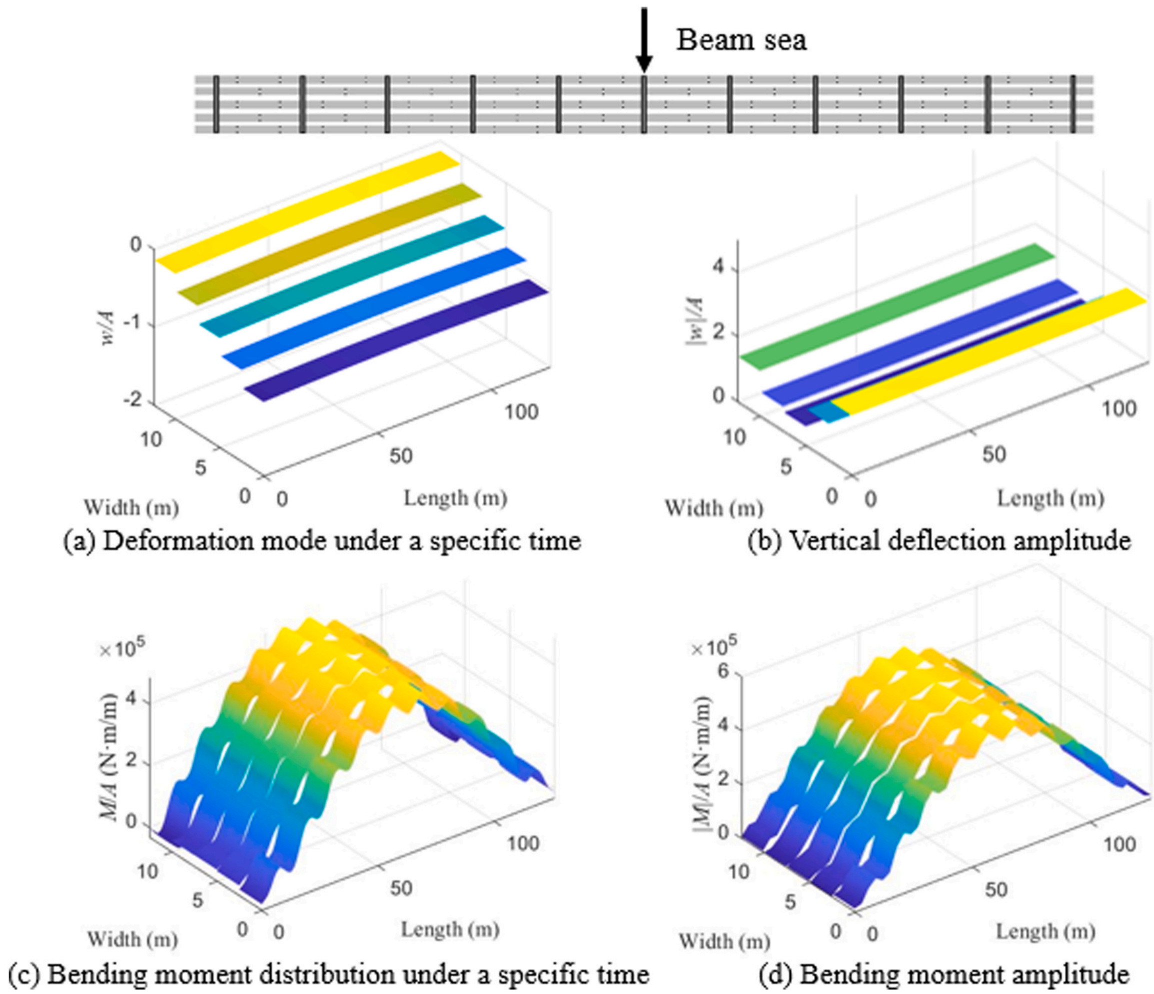

Fig. 14. Hydroelastic responses of assembled floating structure in a unit beam sea: (a) and (b) vertical deflection; (c) and (d) bending moment response.

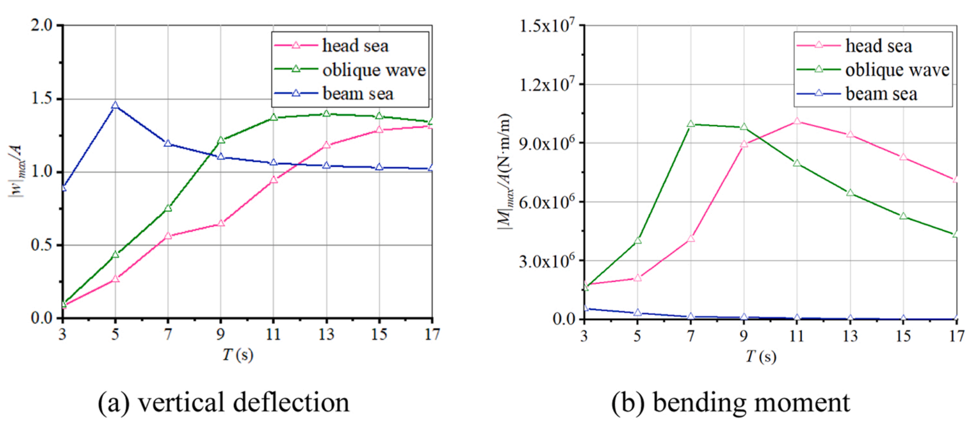

Fig. 15. Structural responses under different wave directions and wave periods (water depth = 15 m).

difference. In addition, the concrete tubes are represented with plane instead of circular section. Although it is shown as a surface discontinuity in Fig. 13 (a), the actual surface of tubes can still be formed as a flat surface. Vertical deflection amplitude in the transverse direction is high on both sides while low in the middle. The maximum deflection amplitude reaches 1.85, which is significantly larger than that in the case of head sea and oblique wave. The peak amplitude of bending moment response under transverse waves is low at 4.8×10^5 N·m/m. The analyses above indicate that oblique waves represent the most hazardous wave condition. Further investigation into other wave conditions and water depth on hydroelastic response of the structure will be conducted in subsequent sections.

4.4.3. *Influence of wave period*

The hydroelastic response to a 4 s wave is discussed in the preceding section. However, the structure will be exposed to broader wave periods during operation. Hydroelastic analysis is conducted over wave periods ranging from 3 to 17 s, corresponding to incident wavelength between

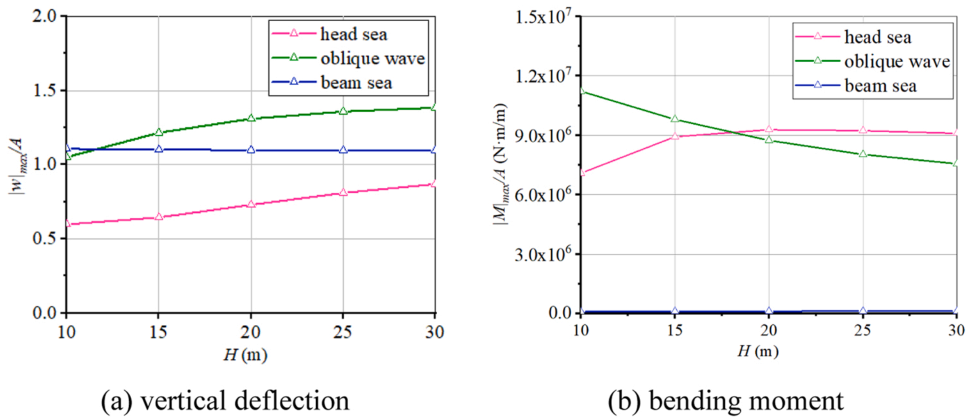

Fig. 16. Structural responses under different water depths (wave period = 9 s).

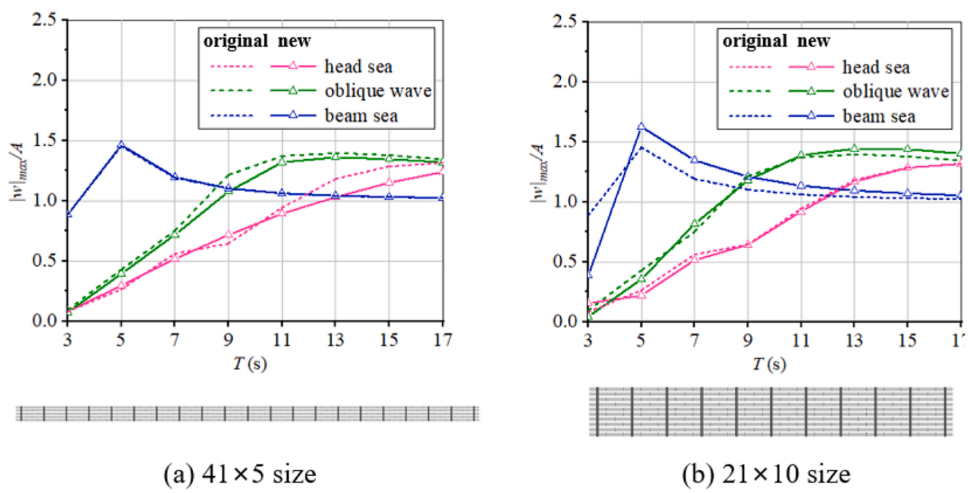

Fig. 17. Structural vertical deflection responses of different size structures (solid lines for new structures and dashed lines for former structure).

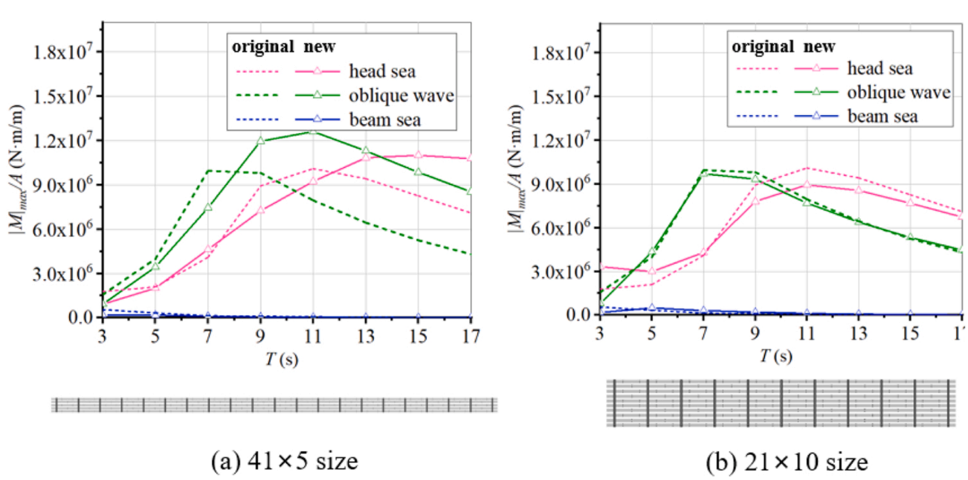

Fig. 18. Structural bending moment responses of different size structures (solid lines for new structures and dashed lines for former structure).

14.0 to 198.9 m. Under each wave period, the maximum value in all the nodes is taken as the structural response amplitude. Fig. 15 shows the structural response amplitudes under different wave directions and wave periods, Fig. 15 (a) and (b) for vertical deflection and bending moment respectively.

The effect of wave period on vertical deflection is mainly concentrated in the short periods less than 9 s. The structure is more sensitive to beam sea in short periods, and the vertical deflection amplitude reaches a peak value of 1.45 in 5 s wave. For long-period waves higher than 11 s, the effects of wave period and wave direction on vertical deflection amplitude are no longer significant. Structural moment response amplitudes under head sea and oblique wave are significantly larger than those under beam sea. The peaks under head sea and oblique wave are close to each other but occur at different wave periods. This

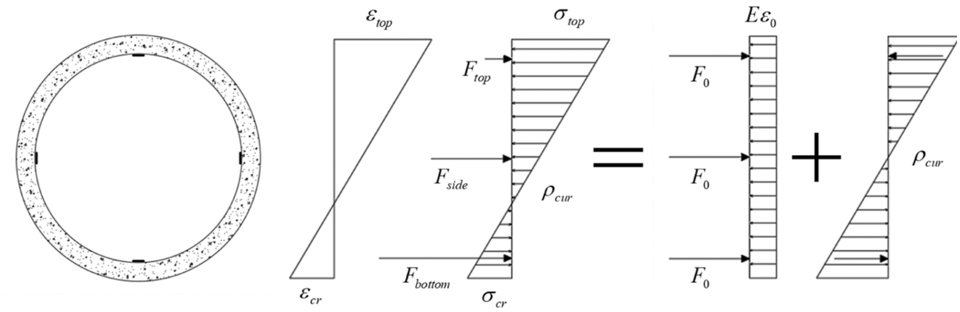

Fig. 19. Strain and stress distribution on the cross-section of a CFRP prestressed concrete tube.

phenomenon of different sensitivity periods has been observed in similar structures[22], which is due to the difference in longitudinal and oblique dimension. The sensitivity period under head sea is around 11 s, whereas that under oblique wave is around 7 s. Overall, when the angle between wave direction and longitudinal direction is less than 45°, the effect on structural response is limited. However, as the angle increases to 90°, a significant difference is observed.

4.4.4. Influence of water depth

The structure is planned to operate in a water depth of 10 – 30 m. Consequently, it is imperative to conduct an analysis considering the influence of varying water depths. When the wave enters shallow water from deep water, wavelength becomes shorter and wave speed decreases, thus the structural response changes. Regarding the influence rule of wave period, the most sensitive wave period 9 s is selected for water depth analysis, and the results are shown in Fig. 16. The effect of water depth on structural response is not obvious. Under oblique wave, vertical deflection is positively correlated with water depth, while bending moment is inversely correlated with water depth.

4.4.5. Influence of structural dimension

In practical use, structures may be designed in different sizes, so the applicability of the new structural model to various structural dimensions needs to be verified. Increase the above structural dimension (21 *5 tubes) to double length (42 *5 tubes) and double width (21 *10 tubes). The hydroelastic responses of the new structures are also studied with the wave range of 3 – 17 s and three wave directions, as shown in Fig. 17 and Fig. 18. The responses of new structures and the original structure are represented by solid and dashed lines, respectively.

Learned that the vertical deflections of the new and original structures show similar trends. The change in vertical deflection amplitude after dimensional change is in the range of 12 %. Bending moment response amplitude is more sensitive to length. After doubling the length, the sensitive period and peak response of the structure under both head sea and oblique wave increase. The maximum moment response amplitude increases by 8.9 % under head sea and 26.6 % under oblique wave. Whereas, after doubling the width, the sensitive period and the peak response remain almost unchanged.

5. Structural analysis

In this section, the bending moment in hydroelastic response calculated above is checked. It is assumed that the structural behavior under normal wave loads satisfies the plane-section assumption and the concrete is in elastic state. The contribution of GFRP rebars to the cracking load is ignored due to the similar elastic modulus to concrete. The strain and stress distributions in the concrete tube section under cracking load are shown in Fig. 19. ε_{cr}, σ_{cr} and, ε_{top}, σ_{top} are the strain and stress for concrete cracking and tube topside, respectively. F_{top} and F_{bottom} represent the forces in the top and bottom CFRP cables.

Stress state of the prestressed tube under bending moment can be combined by two modes, a prestressed tube and a tube under bending moment. In the first mode, no bending moment exists in the concrete tube. In the second mode, neutral plane is the middle plane due to the symmetry of cross-section. Additionally, the curvature of the second mode is the same as prestressed tube. The following equations can be obtained through strain compatibility:

$$F_{top} = F_0 - E_{\mathrm{CFRP}}A_{\mathrm{CFRP}}\left(\frac{d}{2\rho_{cur}}\right) \tag{51}$$

$$F_{bottom} = F_0 + E_{\mathrm{CFRP}}A_{\mathrm{CFRP}}\left(\frac{d}{2\rho_{cur}}\right) \tag{52}$$

$$F_{side} = F_0 \tag{53}$$

where d is the inner diameter and ρ_{cur} is the sectional curvature; ε_0 is the strain in concrete after CFRP cable post-tension; F_0 is the prestress force in CFRP cable; E_{CFRP} and A_{CFRP} are the elastic modulus and cross-section area of CFRP cable.

By combining two modes, the cracking strain can be expressed as follows:

$$\varepsilon_{cr} = \varepsilon_0 + \frac{D}{2\rho_{cur}} \tag{54}$$

ε_{cr} is assumed to be 100 με for concrete, and ρ_{cur} is obtained by Eq. (54). The cracking bending moment is equal to that of the second mode, which is:

$$M_{cr} = \frac{EI}{\rho_{cur}} + E_{\mathrm{CFRP}}A_{\mathrm{CFRP}}\left(\frac{d}{2\rho_{cur}}\right)d \tag{55}$$

By solving Eq. (55), the cracking bending moment 2.6×10^6 N·m is obtained. Assuming ε_0 equals zero to eliminate CFRP prestress, cracking bending moment is only 1.9×10^6 N·m left. Prestressed CFRP cables increase the cracking bending moment by 37 %. Based on the results in hydroelastic analysis, the safety period of head sea is 3–7 s and the safety period of oblique wave is 3–5 s under 1 m wave height. The structure is suitable for calm sea conditions in harbours, where long-period waves are suppressed and wave heights are reduced by breakwaters. To make the structure suitable for harsher wave conditions, the length of the structure can be appropriately reduced. Additionally, increasing the prestress in concrete tubes can help postpone cracks during higher waves. Furthermore, even when the structure is exposed to rare extreme waves, this new structure is designed to be able to float with the bellow even after the concrete tubes crack.

(a) Raft WEC [28] (b) Structure concept

Fig. 20. BRT-FS with WEC hinged connections.

6. Discussion

In the structure component aspects, a large proportion of mature industrial products improves the feasibility of BRT-FS. In the construction aspects, the production of concrete tubes can follow the production process of existing drainage tubes, which also improves the feasibility of BRT-FS. In the mechanical property aspects, the feasibility of normal service under expected working conditions is verified by the calculation mentioned above. As a consequence, the novel BRT-FS can satisfy the nearshore demand including tourism, marine aquaculture, photovoltaic power generation, and so on.

Compared with traditional VLFS, BRT-FS has the following advantages:

- High designability. Diverse shapes and sizes can be designed using small size modules. The structure can be easily expanded or reinforced locally using filament winding to meet special utilization requirements.
- Excellent durability. The main load-bearing components realize "no steel", which can prolong service life and reduce maintenance costs. Moreover, concrete tubes can be recycled conveniently due to modularization.
- Low crack control requirement. The separation of stress and sealing demands can ease design and improve safety. Concrete tubes and bellows function as load-bearing and sealed buoyancy elements respectively, which avoids the floating structures still needing to ensure their sealing performance even under extreme loading conditions.
- High construction efficiency. The production method for concrete tubes is mature and effective, enabling mass production. Additionally, concrete tubes can be transported by trains or vessels, then swiftly installed in dock or offshore.

A further design of this structure with power generation system is also proposed here. It is proved that hinge connections in multi-module configuration can reduce structural hydroelastic response[32,37]. A raft wave energy converter (WEC) shows a similar configuration, which can convert rotation movement between rafts into electricity, as shown in Fig. 20 (a)[6,28]. Combining these two concepts, BRT-FS with WEC hinged connections is formed as shown in Fig. 20 (b). This concept is more environment-friendly which can partially realize self-supply.

7. Conclusions

Inspired by bamboo rafts, a novel BRT-FS assembled by FRP reinforced concrete tubes is proposed in this paper. It has good designability and construction efficiency due to its unique structural design. The durability is improved by the addition of two corrosion-resistant materials, concrete and FRP. The bearing and buoyancy functions are separated to further increase the durability of the structure and ease structural design. Based on existing models, a new hydroelastic model for the novel structure is proposed, whose accuracy is verified. Then structural responses under different wave directions, wave periods, water depth, and structural dimensions are analyzed to find hydroelastic response characteristics. Moreover, the cross-section bearing capacity of the concrete tube is calculated to find use condition for BRT-FS. Based on the analysis results, the following conclusions can be drawn:

1. The simplified model proposed for BRT-FS demonstrates reliability and convergence. The hydrodynamic effect of a circular section is taken into account through the vertical projection of fluid action. The calculation results indicate that the hydroelastic behavior of circular section closely resembles that of square section.
2. BRT-FS will behave different responses under different wave directions. Under head sea, the vertical deflection amplitude is minimal in the middle, while bending moment amplitude reaches maximum at the same location. The vertical deflection distributions under oblique wave and beam sea are different from that under head sea. However, the bending moment distributions remain similar. The maximum vertical deflection response and bending moment response both increase under oblique wave. Under beam sea, the maximum vertical deflection response increase, while the maximum bending moment response decrease.
3. Both vertical deflections and bending moments exhibit similar trends with wave periods in the head sea and oblique wave. These two wave directions have similar peak values, but different sensitive periods. The sensitivity period under head sea is around 11 s, whereas that under oblique wave is around 7 s. The vertical deflection under 5 s beam sea reaches its maximum, while the bending moment is always of a small order of magnitude.
4. Water depth and transverse dimension have no significant influence on the structural response. But an increase in length results in higher peak response and larger sensitive period. The length of the structure needs to be controlled if the applied wave condition is poor.
5. The structural analysis of the section bearing capacity show that the safety period of head sea is 3-7 s and the safety period of oblique wave is 3-5 s under 1 m wave height, which is a clam harbour sea condition. To make the structure suitable for harsher wave conditions, breakwater can be incorporated to suppress high-period wave and reduce wave heights. Furthermore, even when the structure is exposed to rare extreme waves, this new structure is designed to be able to float with the bellow even after the concrete tubes crack. The separation of load-bearing and buoyant functions ensures structural safety and ease of design.

Conclusively, the novel BRT-FS has broad application perspectives in offshore construction due to its high corrosion resistance, designability, construction efficiency, and low crack control requirement. Structural details such as tube-tube joints, tube-beam joints, CFRP cable anchorages, and shear capacity will be further designed and tested in the future.

CRediT authorship contribution statement

Chongfeng Xie: Writing – original draft, Validation, Methodology, Investigation, Formal analysis, Data curation. **Peng Feng:** Writing – review & editing, Supervision, Resources, Project administration, Methodology, Funding acquisition, Conceptualization.

Declaration of Competing Interest

The authors declare that they have no known competing financial interests or personal relationships that could have appeared to influence the work reported in this paper.

Data availability

Data will be made available on request.

Acknowledgments

This research has been supported by the National Key Research and Development Program of China (No. 2022YFC3801800), the National Natural Science Foundation of China (No. U2106219), and the New Cornerstone Science Foundation through the XPLORER PRIZE. The first author Chongfeng Xie was supported by the Program Fund of Non-Metallic Excellence and Innovation Center for Building Materials (No. 2023Ph. D-1).

References

[1] Ai P, Feng P, Lin H, Zhu P, Ding G. Novel self-anchored CFRP cable system: concept and anchorage behavior. Compos Struct 2021;263. https://doi.org/10.1016/j.compstruct.2021.113736.

[2] Al-Khafaji AF, Haluza RT, Benzecry V, Myers JJ, Bakis CE, Nanni A. Durability assessment of 15- to 20-year-old GFRP Bars extracted from bridges in the US. II: GFRP bar assessment. J Compos Constr 2021;25(2). https://doi.org/10.1061/(asce)cc.1943-5614.0001112.

[3] Alabtah FG, Mahdi E, Eliyan FF. The use of fiber reinforced polymeric composites in pipelines: a review. Compos Struct 2021;276. https://doi.org/10.1016/j.compstruct.2021.114595.

[4] Benzecry V, Al-Khafaji AF, Haluza RT, Bakis CE, Myers JJ, Nanni A. Durability assessment of 15- to 20-year-old GFRP Bars extracted from bridges in the US. I: selected bridges, bar extraction, and concrete assessment. J Compos Constr 2021; 25(2). https://doi.org/10.1061/(asce)cc.1943-5614.0001110.

[5] Dai J, Hellan Ø, Watn A, Ang KK. Modular Multi-purpose Floating Structures for Space Creation. WCFS2020. Singapore: Springer Singapore; 2022. p. 257–71.

[6] Davey T, Sarmiento J, Ohana J, Thiebaut F, Haquin S, Weber M, et al. Round robin testing: exploring experimental uncertainties through a multifacility comparison of a hinged raft wave energy converter. J Mar Sci Eng 2021;9(9). https://doi.org/10.3390/jmse9090946.

[7] Guades E, Aravinthan T, Islam M, Manalo A. A review on the driving performance of FRP composite piles. Compos Struct 2012;94(6):1932–42. https://doi.org/10.1016/j.compstruct.2012.02.004.

[8] Gulas S, Downton M, D'Souza K, Hayden K, Walker TR. Declining arctic ocean oil and gas developments: opportunities to improve governance and environmental pollution control. Mar Policy 2017;75:53–61. https://doi.org/10.1016/j.marpol.2016.10.014.

[9] Habeeb MN, Ashour AF. Flexural behavior of continuous GFRP reinforced concrete beams. J Compos Constr 2008;12(2):115–24. https://doi.org/10.1061/(ASCE)1090-0268(2008)12:2(115).

[10] Helland K., Jensen B., Martin J., Meaas P. The Troll Oil Floater: The First Concrete Floater Platform. The Fourth International Offshore and Polar Engineering Conference.1994. p. ISOPE-I-94-303.

[11] Helland S, Aarstein R, Maage M. In-field performance of North Sea offshore platforms with regard to chloride resistance. Struct Concr 2010;11(1):15–24. https://doi.org/10.1680/stco.2010.11.1.015.

[12] Jiang D, Tan KH, Dai J, Ang KK, Nguyen HP. Behavior of concrete modular multi-purpose floating structures. Ocean Eng 2021;229. https://doi.org/10.1016/j.oceaneng.2021.108971.

[13] Jiang D, Tan KH, Dai J, Ong KCG, Heng S. Structural performance evaluation of innovative prestressed concrete floating fuel storage tanks. Struct Concr 2019;20(1):15–31. https://doi.org/10.1002/suco.201800032.

[14] Jiang D, Tan KH, Wang CM, Ong KCG, Bra H, Jin J, et al. Analysis and design of floating prestressed concrete structures in shallow waters. Mar Struct 2018;59: 301–20. https://doi.org/10.1016/j.marstruc.2018.01.006.

[15] Kafodya I, Xian G, Li H. Durability study of pultruded CFRP plates immersed in water and seawater under sustained bending: water uptake and effects on the mechanical properties. Compos Part B: Eng 2015;70:138–48. https://doi.org/10.1016/j.compositesb.2014.10.034.

[16] Kaiser MJ, Snyder B, Yu Y. A review of the feasibility, costs, and benefits of platform-based open ocean aquaculture in the Gulf of Mexico. Ocean Coast Manag 2011;54(10):721–30. https://doi.org/10.1016/j.ocecoaman.2011.07.005.

[17] Karperaki AE, Belibassakis KA. Hydroelastic analysis of very large floating structures in variable bathymetry regions by multi-modal expansions and FEM. J Fluids Struct 2021;102. https://doi.org/10.1016/j.jfluidstructs.2021.103236.

[18] Koekoek M. Connecting modular floating structures. Gemeente Rotterdam: Netherlands. 2010.

[19] Kyoung JH, Hong SY, Kim BW, Cho SK. Hydroelastic response of a very large floating structure over a variable bottom topography. Ocean Eng 2005;32(17): 2040–52. https://doi.org/10.1016/j.oceaneng.2005.03.003.

[20] Li G, Hou C, Shen L. Life-cycle analysis of FRP-strengthened offshore CFST columns suffering from steel corrosion. Compos Struct 2021;277. https://doi.org/10.1016/j.compstruct.2021.114607.

[21] Li J, Wu Z, Shi C, Yuan Q, Zhang Z. Durability of ultra-high performance concrete – A review. Constr Build Mater 2020;255:119296. https://doi.org/10.1016/j.conbuildmat.2020.119296.

[22] Li Z, Chen D, Feng X, Chen J-F. Hydroelastic analysis and structural design of a modular floating structure applying ultra-high performance fiber-reinforced concrete. Ocean Eng 2023;277. https://doi.org/10.1016/j.oceaneng.2023.114266.

[23] Linton CM. Rapidly convergent representations for Green' functions for Laplace' equation. Proc R Soc Lond Ser A: Math, Phys Eng Sci 1999;455(1985):1767–97. https://doi.org/10.1098/rspa.1999.0379.

[24] Liu T, Liu X, Feng P. A comprehensive review on mechanical properties of pultruded FRP composites subjected to long-term environmental effects. Compos Part B: Eng 2020;191. https://doi.org/10.1016/j.compositesb.2020.107958.

[25] Logan DL. First Course in the Finite Element Method, Enhanced Edition, SI Version. Cengage Learning,; 2022.

[26] Nguyen HP, Dai J, Wang CM, Ang KK, Luong VH. Reducing hydroelastic responses of pontoon-type VLFS using vertical elastic mooring lines. Mar Struct 2018;59: 251–70. https://doi.org/10.1016/j.marstruc.2018.02.005.

[27] Pérez Fernández R, Lamas Pardo M. Offshore concrete structures. Ocean Eng 2013; 58:304–16. https://doi.org/10.1016/j.oceaneng.2012.11.007.

[28] Ruol P, Zanuttigh B, Martinelli L, Kofoed JP, Frigaard P. Near-shore floating wave energy converters: applications for coastal protection. 32nd Int Conf Coast Eng ICCE 2011:2010.

[29] Shao W, Sun Q, Xu X, Yue W, Shi D. Durability life prediction and horizontal bearing characteristics of CFRP composite piles in marine environments. Constr Build Mater 2023;367:130116. https://doi.org/10.1016/j.conbuildmat.2022.130116.

[30] Tay ZY. Artificial neural network framework for prediction of hydroelastic response of very large floating structure. Appl Ocean Res 2023;139:103701. https://doi.org/10.1016/j.apor.2023.103701.

[31] Tay ZY, Wang CD, Wang CM. Hydroelastic response of a box-like floating fuel storage module modeled using non-conforming quadratic-serendipity Mindlin plate element. Eng Struct 2007;29(12):3503–14. https://doi.org/10.1016/j.engstruct.2007.08.015.

[32] Teng B., Gou Y., Wang G., Cao G. Motion response of hinged multiple floating bodies on local seabed. The Twenty-fourth International Ocean and Polar Engineering Conference. OnePetro; 2014.

[33] Ueda S. Mooring systems of the world largest floating oil storage base. In: Bratteland E, editor. Advances in Berthing and Mooring of Ships and Offshore Structures. Springer Netherlands; 1988. p. 461–73. https://doi.org/10.1007/978-94-009-1407-0_32.

[34] Wang CD, Meylan MH. A higher-order-coupled boundary element and finite element method for the wave forcing of a floating elastic plate. J Fluids Struct 2004;19(4):557–72. https://doi.org/10.1016/j.jfluidstructs.2004.02.006.

[35] Weaver W, Timoshenko SP, Young DH. Vibration problems in engineering. Wiley,; 1991. https://books.google.com/books?id=YZ7t8LgRqi0C.

[36] Yang H, Zhao S, Kim C. Analysis of floating city design solutions in the context of carbon neutrality-focus on Busan Oceanix City. Energy Rep 2022;8:153–62. https://doi.org/10.1016/j.egyr.2022.10.310.

[37] Yoon J-S, Cho S-P, Jiwinangun RG, Lee P-S. Hydroelastic analysis of floating plates with multiple hinge connections in regular waves. Mar Struct 2014;36:65–87. https://doi.org/10.1016/j.marstruc.2014.02.002.

[38] Zeng J-J, Feng P, Dai J-G, Zhuge Y. Development and behavior of novel FRP-UHPC tubular members. Eng Struct 2022;266. https://doi.org/10.1016/j.engstruct.2022.114540.

[39] Zhang Y, Liu Z, Xin J, Wang Y, Zhang C, Zhang Y. The attenuation mechanism of CFRP repaired corroded marine pipelines based on experiments and FEM. Thin-Walled Struct 2021;169. https://doi.org/10.1016/j.tws.2021.108469.